Complex geometry and kinematics of subsidiary faults within a carbonate-hosted relay ramp.

Marco Mercuri[a*], Ken J. W. McCaffrey[b], Luca Smeraglia[a,c], Paolo Mazzanti[a,d], Cristiano Collettini, C.[a], and Eugenio Carminati[a]

Affiliation addresses:

[a] Dipartimento di Scienze della Terra, Sapienza Università di Roma, Piazzale Aldo Moro 5, 00185, Rome, Italy

[b] Earth Sciences Department, Durham University, South Road, Durham, DH1 3LE, UK

[c] Laboratoire Chrono-Environnement, Université de Bourgogne Franche-Comté, Besançon, France

[d] NHAZCA S.r.l., spin-off company University of Rome "Sapienza", Via Vittorio Bachelet 12, 00185 Rome, Italy

E-mail addresses: marco.mercuri@uniroma1.it (M. Mercuri), k.j.w.mccaffrey@durham.ac.uk (K. J. W. McCaffrey), luca.smeraglia@uniroma1.it (L. Smeraglia), paolo.mazzanti@uniroma1.it (P. Mazzanti), cristiano.collettini@uniroma1.it (C. Collettini), eugenio.carminati@uniroma1.it (E. Carminati).

*corresponding author: tel. +393342844933; e-mail: marco.mercuri@uniroma1.it; postal address: Dipartimento di Scienze della Terra, Sapienza Università di Roma, Piazzale Aldo Moro 5, 000185 Rome, Italy

keywords: carbonate-hosted faults; Digital Outcrop Models; relay ramp; fault kinematics; slip tendency

Abstract

Minor fault geometry and kinematics within relay ramps is strongly related to the stress field perturbations that can be produced when two major fault segments overlap and interact. Here we integrate classical fieldwork and interpretation of a virtual outcrop to investigate the geometry and kinematics of subsidiary faults within a relay ramp along the Tre Monti normal fault in the Central Apennines. Although the Tre Monti fault strikes parallel to the regional extension (NE-SW) it shows predominant dip-slip kinematics, suggesting a NW-SE oriented extension acting at sub-regional scale (1-10 km). Conversely, the slickenlines collected on the front segment of the relay ramp highlight right-lateral kinematics. The subsidiary faults in the relay ramp show a complex geometry (variable attitudes) and slickenlines describe multiple kinematics (left-lateral, dip-slip, right-lateral), independently of their orientation. Our fault slip analysis indicates that a local stress field retrieved from the kinematic inversion of the slickenlines collected on the front segment, and likely promoted by the interaction between the overlapping fault segments that bound the relay zone, can explain most of the geometry and kinematics of the subsidiary faults. Further complexity is added by the temporal interaction with both the regional and sub-regional stress fields.

1. Introduction

Relay ramps transfer displacement between two overlapping fault segments and are common in extensional tectonic regimes (e.g., Larsen, 1988, Peacock and Sanderson, 1991, 1994). They form in response to the mechanical interaction between the overlapping faults causing the tilting of beds, producing strong damage and, eventually, the linkage between the fault segments (Peacock & Sanderson, 1994; Fossen and Rotevatn, 2016 and references therein). Relay ramps (and interaction damage zones in general; e.g., Peacock et al., 2017) are characterized by stronger damage and by subsidiary faults and fractures having a wider range of orientations than isolated fault segments (Kattenhorn et al., 2000; Peacock et al., 2000; Peacock and Parfitt, 2002; Fossen et al., 2005; Çiftci & Bozkurt, 2007; Bastesen and Rotevatn, 2012; Long & Imber, 2012). The strong damage and the structural complexity in zones of fault interaction can have important consequences on fluid flow, leading to enhanced permeability (e.g., Berkowitz, 1995) and to a multi-directional migration of fluids, including hydrocarbons, CO_2, ground water, and hydrothermal fluids (Sibson, 1996; Curewitz and Karson, 1997; Rowland and Sibson, 2004; Rotevatn et al., 2009; Dockrill and Shipton, 2010; Fossen and Rotevatn, 2016). Since about the half of the current hydrocarbon reserves are held within carbonates, carbonate-hosted relay ramps represent a very interesting case study.

The variability in subsidiary structural orientations, including joints and normal faults striking orthogonally to the main fault segments (e.g., Kattenhorn et al., 2000; Ciftci & Bozkurt, 2007), can be very important for cross-fault fluid migration, increasing the chance of some fractures and faults being optimally oriented to open and/or slip under various stress fields (Fossen & Rotevatn, 2006). The presence of variably oriented faults and fractures is commonly attributed to local stress field perturbations due to the interaction and progressive linkage between the fault segments that border the relay ramp, or to the development of the relay ramp itself (Crider & Pollard, 1998; Kattenhorn et al., 2000; Bastesen & Rotevatn, 2012). The existence of various controlling factors (e.g., the displacement profiles, relative orientations, and growth rates of the interacting faults; Fossen and Rotevatn, 2016), makes it difficult to constrain the local stress field within a relay ramp. Although attempts have been made to model the stress field within a relay ramp (e.g., Crider and Pollard, 1998) its better characterization through field observations conducted on exhumed faults can help predicting faults and fractures orientations, with important consequences to the assessment of fluid flow within fault zones.

In the present work, we combined traditional fieldwork and virtual outcrop interpretation (Bellian et al., 2005; McCaffrey et al., 2005a,b; Hodgetts, 2013) to investigate the geometry and kinematics of the subsidiary faults within a portion of a carbonate-hosted relay ramp pertaining to the Tre Monti fault, a normal fault in the Central Apennines of Italy. The fault slip analysis shows that a local stress field retrieved from the kinematic inversion of the slickenlines locally observed on the front segment of the relay ramp is able to explain most, but not all, of the complex geometry and kinematics of the subsidiary faults. Transient effects of regional and sub-regional stress fields acting on the relay ramp structure may explain this complexity.

2. Geological setting

The central Apennines are a late-Oligocene to present fold-and-thrust belt that formed in response to the westward directed subduction of the Adria plate under the European plate (Doglioni, 1991). This produced a north-eastward migrating and NE-SW directed shortening which was accommodated by thrusts (Fig. 1a). The thrusts scraped off the sedimentary sequence overlying the continental basement of Adria (Patacca et al., 2008), including a thick carbonate succession that had been deposited since the late-Triassic to middle Miocene time (Cosentino et al., 2010 and references therein). In the study area (Fucino basin) the thrusting events occurred from late Miocene to early Pliocene (Cavinato and De Celles, 1999) whilst the presently active compressive front is located ~ 60 km towards the NE.

Since the early Pliocene, extensional tectonics have affected the central Apennines in response to the opening of the Tyrrhenian back-arc basin (Doglioni, 1991) and, as testified by stress maps (Montone et al., 2004; Heidbach et al., 2016), GPS measurements (D'Agostino et al., 2001; Devoti et al., 2010), and focal mechanisms of earthquakes (Scognamiglio et al., 2010; Chiaraluce, 2012; Chiaraluce et al., 2017), is still ongoing. In particular, NE-SW oriented extension and uplift is accommodated by extensional faults, which dismember the shallow-water to pelagic carbonate succession that constitutes the backbone of the Central Apennines, generating several intermontane basins (Fig. 1a; e.g., Fucino, Sulmona, L'Aquila, Campo Imperatore) (Cosentino et al., 2010). The extensional faults bordering the intermontane basins mostly strike NW-SE, although rare SW-NE trending fault, such as the Tre Monti fault, are present (Fig. 1a). In this tectonic framework, the Tre Monti extensional fault marks the north-western boundary of the Fucino Basin and crops out for ~ 7 km through a series of right-stepping SE-dipping fault scarps (Fig. 2a).

The reconstruction of Pliocene-Quaternary tectonic structures of the Fucino basin (Galadini and Messina, 1994, 2001; Cavinato et al., 2002; Gori et al., 2017) is based on the increasing thickness of Pliocene deposits towards the northern sector of the basin (Cavinato et al., 2002). The tectonic evolution of the Fucino basin during early Pliocene time was initially controlled by dip-slip movements along the Tre Monti fault, which was longer at the time (Fig. 1b), with the consequent formation of a NE-SW elongated semi-graben. Since Late Pliocene, the Fucino basin tectonics was controlled by NW-SE striking faults that border the Fucino basin to the NE (Cavinato et al., 2002), which cut and displaced the Tre Monti fault near the Celano village (Fig. 1c).

The main fault scarps of the Tre Monti fault juxtapose Pliocene to Holocene continental deposits in the hangingwall and early Cretaceous to middle Miocene shallow water carbonates in the footwall (Fig. 2a, b). Interpreted seismic reflection profiles (Cavinato et al., 2002; Smeraglia et al., 2016) show that the throw increases from ~800 m up to ~ 2,000 m moving from SW to NE. The exposed portion of the Tre Monti fault was exhumed from depth < 3 km (Smeraglia et al., 2016). The slickenlines on the fault scarps indicate mainly dip-slip kinematics, although rare right-lateral movements are locally recorded (Morewood and Roberts, 2000; Smeraglia et al., 2016). The Linked Bingham fault plane solution for these kinematic indicators indicate NW-SE oriented tension (Fig. 2a), i.e., orthogonal to regional NE-SW extension. Paleoseismological investigations with cosmogenic ^{36}Cl measurements on fault scarps (Benedetti et al., 2013; Cowie et al., 2017) suggest that the Tre Monti fault has been active between Early Pliocene and recent times with dip-slip kinematics. The occurrence of predominantly dip-slip movements on a fault striking nearly parallel to the regional extension vector has been explained by invoking a release fault geometry for the Tre Monti fault (Destro, 1995; Galadini and Messina, 2001). In this scenario the Tre Monti fault accommodates a differential throw along the strike of the NW-SE striking fault system that borders the Fucino basin to the NE and comprises the San Potito-Celano, Celano-Pescina, and Serrone faults (hereafter the San Potito–Serrone fault system, SPSFS; see Fig. 1a,c). Finally, microstructural analyses performed on the fault core suggest that the TMF experienced past earthquakes. This is

testified by some seismic slip indicators found in the fault core: fluidized ultracataclasite layers, injection veins, and decomposed calcite crystals (Smith et al., 2011; Smeraglia et al., 2016, 2017).
In this work we focus on a key outcrop, represented by an abandoned quarry (the "La Forchetta" quarry in Smeraglia et al., 2016), located ~ 2 km WSW of Celano (42°04'35''N 13°30'00''E; Fig. 2).

3. Methods

We combine traditional fieldwork with the interpretation of a virtual outcrop to investigated minor faults within the damage zone of the study area. Using traditional fieldwork methods, we have (1) collected orientation data for the subsidiary faults to provide control on the virtual outcrop fault data and, (2) collected slickenline data to enable a kinematic analysis.

3.1. Virtual outcrop acquisition

The virtual outcrop consists of a high-resolution point cloud that has been collected through a terrestrial laser scanner (TLS) survey (Fig. 3).
To build the point cloud, the TLS records the time-of-flight of a series of laser pulses reflected by the outcrop surface (thousands of measurements per second). The TLS calculates the distance between the sensor and the outcrop knowing the velocity of the light. Knowing the exact position (absolute geographic coordinates) of some ground control points (GCP) in the scene, all distance measurements relative to the TLS instrument are then converted to a point cloud, where each point is identified by X, Y, Z values representing its geographic coordinates. The integration of the laser scanner device with images from a calibrated high-resolution camera (Fig. 3) enables true colours to be added to the scene. Consequently, RGB values are assigned to each point (White and Jones, 2008) to obtain a georeferenced and true-colour point cloud (Fig. 3). The reader is referred to the papers of Buckley et al., (2008) and Telling et al., (2017) for an extensive review of the terrestrial laser scanner methodology and its application in geology.

For this study we collected high-resolution point clouds from 4 different scan positions using a Riegl VZ1000 instrument (Fig. 3). During the point cloud acquisition, we used 7 ground control points (GCP) with known absolute coordinates. The absolute coordinates of the GCPs were obtained through a differential GPS survey performed using a Leica GX1230 GPS receiver. The point clouds were georeferenced and combined to obtain a single point cloud covering the whole quarry. The final result is a high-resolution (~ 100 million points) true-colour point cloud (Fig. 3).

3.2. Minor faults mapping on the virtual outcrop

Starting from a 3D model (Fig. 3), we constructed a map and a cross section illustrating the minor faults distribution in the quarry. We built the 3D model using the Move™ software, combining a topographic model of the abandoned quarry with a structural interpretation representing the minor faults distribution. Both the topographic model and the structural interpretations were extracted from the point cloud using the CloudCompare software (www.cloudcompare.org).

The topographic model is made up of a Digital Terrain Model combined with an orthophoto of the abandoned quarry. Both have been extracted by converting the point cloud to raster files containing the elevation and RGB values with a grid resolution of 0.5 m steps. The two raster files have been subsequently merged using the Move software.

The structural interpretation was produced by manual picking all visible minor faults in the quarry using the Compass plugin in CloudCompare (Thiele et al., 2017). For each minor fault we have drawn a polyline representing its trace in the quarry topography and, eventually, a zig-zag polyline to include as much of the visible minor fault surfaces as possible (Fig. 4), as described in Pless et al., (2015). In order to produce a polygon and to obtain the attitude of minor faults, all the polylines pertaining to each fault have been fitted with planes using the Compass plugin (Thiele et al., 2017). The goodness of fit was evaluated by analysing the Root Mean Square (RMS) value provided by the plugin (Figs. S2 and S3). We finally built a 3D model of the quarry (Fig. 3) exporting the structural interpretation from CloudCompare and merging it with the topographic model using the Move software (Fig. 3).

The minor faults map was produced by combining the topographic model with the polylines representing fault traces and with point data representing fault attitudes. To produce the cross section, we used the Move software to project each fault polygon orthogonally to a vertical section oriented parallel to the main fault dip (156° N) regardless of the orientation of the fault planes.

3.3. Fault slip analysis

We conducted a fault slip analysis on a dataset of 100 minor fault collected in the field. For each minor fault we collected the attitude of the slip surface (strike, dip, dip azimuth) and the slickenlines orientation (trend, plunge, rake). In detail, we evaluated the geometrical and kinematic compatibility of all the minor faults with different hypothetical stress fields.

The geometrical compatibility has been evaluated calculating the normalised slip tendency (Morris et al., 1996; Lisle and Srivastava, 2004; Collettini and Trippetta, 2007; Di Domenica et al., 2014) for each minor fault in a given stress field. The slip tendency (T_s) measures the potential for slip on a weakness plane subjected to a known stress field and is given by (Morris et al., 1996):

$$T_s = \frac{\tau}{\sigma'_n} \qquad (1),$$

where τ and σ'_n are respectively the resolved shear and effective normal stress ($\sigma'_n = \sigma_n - P_f$, where P_f is the pore fluid pressure) on the fault. According to the Amontons' law for fault reactivation ($\tau = \mu \cdot \sigma'_n$), the condition for slip on a fault is:

$$T_s = \frac{\tau}{\sigma'_n} > \mu_s \qquad (2),$$

where μ_s represents the coefficient of sliding friction. The resolved shear and effective normal stresses on a fault depend on (1) its orientation in the principal stresses reference frame, (2) on the differential stress ($\sigma_1 - \sigma_3$), (3) on the pore fluid pressure, and (4) on the stress shape ratio $\Phi = \frac{(\sigma_2 - \sigma_3)}{(\sigma_1 - \sigma_3)}$. However, within a crustal volume, the differential stress and the pore fluid pressure are often not well-constrained. We can overcome this problem by assuming that the maximum slip tendency value is reached when the frictional sliding envelope given by the Amontons' law is tangential to the $\square_1\square_3$ Mohr's circle in a $\square$-$\square_{\square}$ space. By such an assumption we are able to evaluate the slip tendency in a mechanical system that depends only on the orientation of the fault within the principal stresses reference frame, on the coefficient of friction, and on the stress shape ratio. We assumed a 0.6 friction coefficient, typical of carbonates (Tesei et al., 2014; Carpenter et al., 2016) and a stress shape ratio of 0.56 (Ferrarini et al., 2015). We refer the reader to the papers by Lisle and Srivastava, (2004) and Collettini & Trippetta (2007) for the complete procedure. In the tangential condition assumption, we evaluate the slip potential of a fault through the normalised slip tendency (Lisle and Srivastava, 2004):

$$\square\square_{\square} = \frac{\square_{\square}}{\square_{\square}^{\square\square\square}} \quad (3),$$

Each fault can have $0 \leq \square\square_{\square} \leq 1$. We define a fault well-oriented if $0.5 \leq \square\square_{\square} \leq 1$, and misoriented if $0 \leq \square\square_{\square} < 0.5$.

Although the normalised slip tendency method enables us to establish whether a fault is prone to slip in a given stress field, it does not predict its kinematics in that stress field. Assuming that slip on a fault occurs along the direction of the resolved shear stress (Wallace, 1951; Bott, 1959), we can evaluate the compatibility of the measured slickenlines within a given stress field. Hence, we calculated the predicted slickenlines orientations for the well-oriented minor faults within the stress field using the software FaultKin (Marrett and Allmendinger, 1990; Allmendinger et al., 2011). Consequently, we calculated the difference ($\Delta\square$) between the observed ($\square_{\square\square\square}$) and the predicted rake ($\square_{\square\square\square\square}$) of the slickenlines on the well-oriented minor faults:

$$\Delta\square = |\square_{\square\square\square} - \square_{\square\square\square\square}| \quad (4),$$

We divided the extensional rake values, going from 0° for left-lateral kinematics to 180° for right-lateral kinematics, into 5 fields with amplitude of 36°. For this reason, we decided to classify the slickenlines as compatible with a certain stress field if $\Delta\square \leq 36°$.

4. Results

4.1. Geometry of the minor faults

The study outcrop is located in the overlap zone between two right stepping segments of the main fault, defining a relay ramp environment (Fig. 2c). The distance between the front and the rear segment (sensu Crider and Pollard, 1998) of the relay ramp is ~ 400 m in map view, whilst the two segments overlap for at least 900 m along strike (Fig. 2c). The quarry is located immediately at the footwall and at the western tip of the front segment (Fig. 2c). The front segment dips moderately toward SE (156° mean dip azimuth) and puts Lower Cretaceous shallow-water limestones at the footwall in contact with Middle Pleistocene subaerial breccias ("Brecce Rosate" Unit; Cavinato et al., 2002) at the hangingwall (Fig. 2c and 4). The slickenlines, well-preserved in the western portion of the quarry (Fig. 4), suggest oblique to right-lateral (mean slickenlines rake 155°) kinematics for the front segment. Such kinematics are compatible with a non-Andersonian stress field characterized by oblique σ_1 and NNE gently plunging σ_3 (Fig. 3). The Lower Cretaceous limestones in the quarry host the fault damage zone, characterized by pervasive fracturing and the presence of various small-displacement (metric to decametric) slip surfaces (i.e., minor faults; Fig. 4).

The manual interpretation of the quarry virtual outcrop allowed us to map the minor faults in the damage zone (Fig. 5). The damage zone is characterized by an intensely fractured carbonate host rock and by the presence of numerous minor faults (Figs. 4 and 5). Minor faults are pervasive and heterogeneously distributed, with the highest concentration in the northern sector (Fig. 5). Their trace length, measured from the DOM, spans from 1 m to 50 m with most of the values comprised between 5 m and 10 m (Fig. S1). The density contour stereoplot representing the poles to the minor faults attitudes measured in the field (stereoplot on the left in Fig. 5) is very similar that obtained from the virtual outcrop (stereoplot on the right in Fig. 5). Both the stereoplots show evidence for two major sets of minor faults. The first set is characterized by orientations similar to the main fault, specifically faults dipping > 55° and striking both E-W and NE-SW (stereoplots in Fig. 5). The most prominent example is provided by a very large (~20 m x 25 m) and undulated fault surface exposed in the northern sector of the quarry (Fig. 5 and 6a). The second set is characterized by slip surfaces striking NW-SE (i.e., orthogonal to the main fault) and dipping > 60° (stereoplot in Fig. 5). This set is particularly evident in the eastern sector of the quarry (Fig. 6b). Notably, our observations did not provide any evidence of systematic cross-cutting relationship between the different sets of faults (Fig. 5).

A cross-section across the quarry allows us to visualize the minor faults distribution, and hence to illuminate the fault zone structure at the outcrop scale (Fig. 6c). The largest minor faults pertaining to the first set (Fig. 5, 6c) are arranged with distances varying from 1-2 m to tens of meters (Fig. 6c). The second set is represented by a relatively high number of minor faults striking orthogonal to the main fault. Other minor faults show strikes similar the main fault and have low dip angles, and rare antithetic faults are also present (Fig. 6c).

4.2. Kinematics of the minor faults

The slickenlines collected on the minor faults indicate complex kinematics (Fig. 7). The density contour plot in Figure 7a shows that slickenlines on minor faults have azimuths in variable directions and plunges that range from horizontal to vertical. However, most of the slickenlines plunge between ~220° (SW) and ~ 320° (NW), with the highest density between 240° and 280° (WSW to W approximately; Fig. 7a). In this range we recognize two main clusters (~270°/35° and ~250°/15°) defining W-E oblique and WSW-ENE sub-horizontal movements respectively, and several minor clusters, including NW-SE and WSW-ENE oblique kinematics, and W-E sub-horizontal movements. Finally, other minor clusters indicate sub-vertical movements with slickenlines pointing mainly toward WSW (~250°), SSE (~165°) and SW (~220°).

This wide range of slickenlines, together with the different orientation of the minor faults, results in variable kinematics, spanning from left lateral, to normal to right-lateral, independently of their orientation (Fig. 7b, c). Furthermore, a double set of slickenlines is sometimes observed on NE-SW and E-W striking faults (inset in Fig. 6b). Overall, a right-lateral slip component is the most recorded kinematic sense (44 %), followed by normal (34%), and left lateral motions (22%) (Fig. 7b). The faults that show a main right-lateral component mostly strike in a W-E direction (~57%) and, secondarily, in a NE-SW direction (~23%) (Fig.7b, c). The same kinematics is recorded also by faults striking NW-SE (13 %), and N-S (~7 %). Normal and left-lateral kinematics are nearly equally distributed for the various fault orientations (Fig. 7b, c). The highest number of faults with normal kinematics strike NE-SW (~ 38%), followed by N-S and W-E striking faults (~24% each) (Fig. 7b, c). Finally, left-lateral slip is mainly associated with E-W (36%) and NW-SE striking (32%) faults (Fig. 7b, c).

5. Discussion

5.1 – Geometry of the subsidiary faults

Our study leverages the employment of a virtual outcrop to provide a very detailed description of minor faults within a portion of a carbonate-hosted relay ramp. The manual interpretation of the virtual outcrop allowed us to reconstruct the exact position of each minor fault in 3D space and we used this information to produce a map (Fig. 5) and a cross-section (Fig. 6c) representing their distribution. Furthermore, we were able to extract orientation data by fitting planes to polylines manually drawn on the 3D traces of the minor faults (Fig. 5). The low RMS and RMS/length values testify the goodness of fit (Figs. S2 and S3). The similarity between the stereoplots representing the minor fault attitudes retrieved from the natural and the virtual outcrops (Fig. 5) is the strongest evidence for the accuracy of the 3D model. Thus, our study further confirms and supports the applicability of analyses derived from virtual outcrops in structural geology problems (Tavani et al., 2014; Seers and Hodgetts, 2016; Vollgger and Cruden, 2016 & Telling et al., 2017 among others) and, in particular, the ability to create a precise 3D geometrical reconstruction at outcrop scales (1:5,000 and higher).

The structural map and the cross section reconstructed in our study (e.g. Fig. 5 and 6c) allow for a detailed characterization of the subsidiary fault geometries within the relay zone. The largest subsidiary faults are arranged in major sub-parallel strands striking sub-parallel to the main fault segments and are accompanied by smaller faults with various orientations including those that strike orthogonally to the main fault (Fig. 6c and stereoplot in Figure 5). The presence of subsidiary faults striking sub-parallel to the main fault segments has been observed for carbonate normal faults at different scales (e.g. Jackson and White, 1989; Agosta and Aydin, 2006; Bonson et al., 2007; Collettini et al., 2014 Valoroso et al., 2014; Demurtas et al., 2016; Smeraglia et al., 2016). Similar faults have been observed within relay ramps formed in basement rocks (e.g., Peacock et al., 2000) and been imaged in seismic reflection profiles (Hus et al., 2006). Nonetheless, our work provides one of the first detailed characterizations of the complex fault pattern (e.g. Figs. 5-7) within a carbonate-hosted relay ramp. The detailed structural mapping (scale 1: 2,000) and the large number of subsidiary faults collected for this study (Fig. 5), allowed us to confirm the geometrical (multiple orientations of subsidiary faults and fractures) that has been observed within relay ramps in a few previous studies (Kattenhorn et al., 2000; Çiftçi & Bozkurt, 2007; Bastesen & Rotevatn, 2012).

5.2 – Kinematics and Dynamics of subsidiary faults

Associated with the complex geometry, the subsidiary faults in the damage zone also show complex kinematics, ranging from strike-slip (either dextral or sinistral) to dip-slip movements, independently from their orientations (Fig. 7b,c), with slickenlines plunging toward a wide range of directions (Fig. 7a). These observations suggest that slip on all the subsidiary faults is not related to a single stress field (e.g., Angelier, 1984).

To explain this complex fault pattern, the first hypothesis to explore is that the complex geometry and kinematics results from the overprinting of two (or more) stress fields related to different tectonic regimes acting in different periods of time. This hypothesis can be easily ruled out. In fact, although some NE-SW and E-W striking faults record two slickenline sets (Fig. 6a), systematic cross-cutting relationships between various sets of minor faults are absent (see Fig. 5).

In the following, we test the hypothesis that complex minor fault geometry and kinematics result from the simultaneous activity and competition of at least 3 stress fields (Fig. 8) induced by: 1) active extension in Central Apennines (regional stress field); 2) the Tre Monti fault activity (fault stress field) and 3) the relay zone (quarry stress-field). We firstly provide geological and geophysical background for each stress field, and then we describe our fault slip analysis.

The axial zone of the Apennines is characterized by an extensional Andersonian stress field with NE-SW oriented σ_3 (regional stress field; Fig. 8a and Table 1), as shown by inversion of focal mechanisms (e.g. Chiaraluce et al., 2017). There is strong evidence for the recent activity of the Tre Monti normal fault in the framework of the active extensional fault system of Central Apennines. This is supported by the predominance of dip-slip slickenlines observed on the main fault scarps (stereoplot in Fig. 2a) and by paleoseismological investigations showing dip-slip kinematics (Benedetti et al., 2013; Cowie et al., 2017). The kinematic inversion of slickenlines measured along the main fault scarps defines a NW-SE orientated extension with a sub-vertical σ_1 (fault stress field; Fig. 8a and Table 1). Finally, in a relay zone, it is well documented that slip and stress distribution within the overlapping segments promote the development of a local stress field (Crider and Pollard, 1998; Kattenhorn et al., 2000; Çiftçi & Bozkurt, 2007; Bastesen & Rotevatn, 2012). For our case study we retrieved the local stress field from kinematic inversion of the right-lateral slickenlines observed on the main fault in the quarry (i.e., the front segment of the relay ramp). This stress-field is characterized by a non-Andersionian orientation of the principal stress axes, with a W-trending oblique σ_1 and NNE trending gently dipping σ_3 (quarry stress field; Fig. 8c and Table 1).

The regional stress field (Fig. 8a, Table 1) used as input for the fault slip analysis show that 51% of minor faults are well-oriented in this stress field, but only 27% of them present compatible slickenlines (Fig. 8a). The regional stress field can only explain the right-lateral kinematics of W-E striking faults and the dip-slip kinematics on NW-SE striking faults (Fig. 8a and Table 2).

The fault stress field (Fig. 8b, Table 1) is able to explain the geometry of a large number of subsidiary faults (72%), however only 15% are well-oriented and have compatible kinematics (Fig. 8b). The fault stress field is able to explain only dip-slip slickenlines on NE-SW oriented minor faults (Fig. 8b and Table 2).

The quarry stress field (Fig. 8c and Table 2) is able to explain the distribution of a very high percentage of minor faults (81%) and a large number of these faults (53%) have slickenlines compatible with this stress field (Fig. 8c). The quarry stress field is able to explain the kinematics of minor faults striking both parallel (right-lateral kinematics on W-E and NE-SW striking faults) and orthogonal to the main fault (left-lateral kinematics on NW-SE striking faults).

Within a relay ramp, complex fault geometries are often associated with mechanical interaction and stress rotation between the overlapping faults (Peacock & Sanderson, 1994; Fossen and Rotevatn, 2016). Our mechanical analysis suggests that in the case study of the Tre Monti fault, further geometrical and kinematic complexity can be added by the temporal competition and interaction of various stress fields. Each stress field can either be responsible of the formation of new faults, renewing the minor faults population and increasing the geometrical complexity, or can promote slip on pre-existing well-oriented faults. In this area of Central Apennines, when the regional stress field prevails, promoting slip on the San Potito-Celano and/or Pescina-Celano faults (Fig. 9a), in the relay zone of the Tre Monti fault, slip is favoured on NW-SE structures with dip-slip kinematics and on W-E striking structures with right-lateral movements. On the contrary, when the stress field associated with the Tre Monti fault prevails (i.e. fault stress field; Fig 9b), slip is favoured on NW-SE oriented structures with dip-slip kinematics.

However, the large number of minor faults that show geometric and kinematic compatibility with the quarry stress field (Fig. 8c) indicate that the majority of the minor structures are due to the interaction between the two main fault strands which creates an oblique dextral kinematics on the relay zone (Fig. 9c). We therefore suggest that the complex geometry and kinematics of the minor faults in the relay ramp of the Tre Monti fault is mainly a result of a local stress field caused by interaction between the overlapping fault segments. Further kinematic complexity can be explained by the transient influence of regional and fault-scale stress fields at the local-scale.

6. Conclusions

Using fieldwork and virtual outcrop technologies, we investigated the subsidiary faults geometry and kinematics within a carbonate-hosted relay ramp. The structural map and cross section reconstructed in our study (scale 1: 2,000 and 1:1,000 respectively) allow for a detailed characterization of the subsidiary faults geometry. The largest subsidiary faults show an orientation that is sub-parallel to the main fault segments accompanied by smaller faults with different attitudes and often striking orthogonally to the main fault. Faults also show a wide range of kinematics (left-lateral, dip-slip, right-lateral) independently of their orientation. Based on fault slip analysis, accounting for both fault geometry and kinematics, we suggest that the complex minor fault geometry and kinematics can be mostly explained by the development of a stress perturbation within the relay zone, resulting from the interaction of the overlapping segments. Further geometrical and kinematic complexity may be interpreted as due to the temporary superposition of either the stress field associated with the slip of the entire Tre Monti Fault or the regional active extension. Our results highlight that the geometry and kinematics of minor faults within relay zones are dependent on stress field interactions across the scales.

Acknowledgements

We thank two anonymous reviewers, whose comments helped to improve the quality of the manuscript. We also thank Andrea Billi, Manuel Curzi, Carolina Giorgetti, Telemaco Tesei, Patrizio Petricca and Fabio Trippetta for fruitful discussions, and Marco Baleani, Angelo Galeandro, and Francesco Mohammadi for their help during the laser scanner survey. The virtual outcrop analysis was carried out in Durham University, Earth Sciences Department during a 2-month internship. We also acknowledge Andrea Bistacchi who developed the slip tendency Matlab toolbox that we used for this study. This research was supported by the Sapienza University of Rome Earth Sciences Department Ph.D. funds and Sapienza Progetti di Ateneo 2017 to EC. KM's work in the Apennines was funded by NERC awards NE/I026715/1 and NE/E016545/1.

References

Agosta, F., Aydin, A., 2006. Architecture and deformation mechanism of a basin-bounding normal fault in Mesozoic platform carbonates, central Italy. Journal of Structural Geology 28, 1445–1467.

Allmendinger, R.W., Cardozo, N., Fisher, D.M., 2011. Structural geology algorithms: Vectors and tensors, Cambridge University Press. Cambridge University Press.

Angelier, J. (1984). Tectonic analysis of fault slip data sets. Journal of Geophysical Research: Solid Earth, 89(B7), 5835-5848.

Barton, C., Zoback, M., 1994. Stress perturbations associated with active faults penetrated by boreholes: Possible evidence for near- complete stress drop and a new technique for stress magnitude measurement. Journal of Geophysical Research: Solid Earth 99, 9373–9390.

Bastesen, E., Rotevatn, A., 2012. Evolution and structural style of relay zones in layered limestone–shale sequences: insights from the Hammam Faraun Fault Block, Suez Rift, Egypt. Geol. Soc. Lond. 169, 477–488.

Bellian, J.A., Kerans, C., Jennette, D.C., 2005. Digital Outcrop Models: Applications of Terrestrial

Scanning Lidar Technology in Stratigraphic Modeling. Journal of Sedimentary Research 75, 166–176.

Benedetti, L., Manighetti, I., Gaudemer, Y., Finkel, R., Malavieille, J., Pou, K., Arnold, M., Aumaître, G., Bourlès, D., Keddadouche, K., 2013. Earthquake synchrony and clustering on Fucino faults (Central Italy) as revealed from in situ 36Cl exposure dating. Journal of Geophysical Research: Solid Earth 118, 4948–4974.

Berkowitz, B., 1995. Analysis of fracture network connectivity using percolation theory. Math. Geol. 27, 467–483.

Bistacchi, A., Massironi, M., Menegon, L., Bolognesi, F., Donghi, V., 2012. On the nucleation of non-andersonian faults along phyllosilicate-rich mylonite belts. Geol. Soc. Lond. Spec. Publ. 367 (1), 185-199

Bonson, C.G., Childs, C., Walsh, J.J., Schöpfer, M.P.J., Carboni, V., 2007. Geometric and kinematic controls on the internal structure of a large normal fault in massive limestones: The Maghlaq Fault, Malta. Journal of Structural Geology 29, 336–354.

Bott, M., 1959. The Mechanics of Oblique Slip Faulting. Geological Magazine 96, 109–117.

Buckley, S.J., Howell, J.A., Enge, H.D., Kurz, T.H., 2008. Terrestrial laser scanning in geology: data acquisition, processing and accuracy considerations. Journal of the Geological Society 165, 625–638.

Carpenter, B. M., Collettini, C., Viti, C., & Cavallo, A. (2016). The influence of normal stress and sliding velocity on the frictional behaviour of calcite at room temperature: insights from laboratory experiments and microstructural observations. Geophysical Journal International, 205(1), 548-561.

Cavinato, G. P., Carusi, C., Dall'Asta, M., Miccadei, E., & Piacentini, T. (2002). Sedimentary and tectonic evolution of Plio–Pleistocene alluvial and lacustrine deposits of Fucino Basin (central Italy). Sedimentary Geology, 148(1-2), 29-59.

Cavinato, G.P., De Celles, P.G., 1999. Extensional basins in the tectonically bimodal central Apennines fold-thrust belt, Italy: response to corner flow above a subducting slab in retrograde motion. Geology 27, 955–958.

Chiaraluce, L., 2012. Unravelling the complexity of Apenninic extensional fault systems: A review of the 2009 L'Aquila earthquake (Central Apennines, Italy). Journal of Structural Geology 42, 2–18.

Chiaraluce, L., Stefano, D.R., Tinti, E., Scognamiglio, L., Michele, M., Casarotti, E., Cattaneo, M., Gori, D.P., Chiarabba, C., Monachesi, G., Lombardi, A., Valoroso, L., Latorre, D., Marzorati, S., 2017. The 2016 Central Italy Seismic Sequence: A First Look at the Mainshocks, Aftershocks, and Source Models. 88, 757–771.

Çiftçi, N. B., & Bozkurt, E. (2007). Anomalous stress field and active breaching at relay ramps: a field example from Gediz Graben, SW Turkey. Geological Magazine, 144(4), 687-699.

Collettini, C., Carpenter, B.M., Viti, C., Cruciani, F., Mollo, S., Tesei, T., Trippetta, F., Valoroso, L., Chiaraluce, L., 2014. Fault structure and slip localization in carbonate-bearing normal faults: An example from the Northern Apennines of Italy. Journal of Structural Geology 67, 154–166.

Collettini, C., Trippetta, F., 2007. A slip tendency analysis to test mechanical and structural control on aftershock rupture planes. Earth and Planetary Science Letters 255, 402–413.

Cosentino, D., Cipollari, P., Marsili, P., Scrocca, D., 2010. Geology of the central Apennines: a regional review. 36.

Cowie, P., Phillips, R., Roberts, G., McCaffrey, K., Zijerveld, L., Gregory, L., Walker, F.J., Wedmore, L., Dunai, T., Binnie, S., Freeman, S., Wilcken, K., Shanks, R., Huismans, R., Papanikolaou, I., Michetti, A., Wilkinson, M., 2017. Orogen-scale uplift in the central Italian Apennines drives episodic behaviour of earthquake faults. Scientific Reports 7, 44858.

Crider, J.G., Pollard, D.D., 1998. Fault linkage: Three- dimensional mechanical interaction between echelon normal faults. Journal of Geophysical Research: Solid Earth 103, 24373–24391.

Curewitz, D., Karson, J.A., 1997. Structural settings of hydrothermal outflow: fracture permeability maintained by fault propagation and interaction. J. Volcanol. Geotherm. Res. 79, 149–168

D'Agostino, N., Giuliani, R., Mattone, M., Bonci, L., 2001. Active crustal extension in the Central Apennines (Italy) inferred from GPS measurements in the interval 1994–1999. Geophysical Research Letters 28, 2121–2124.

Demurtas, M., Fondriest, M., Balsamo, F., Clemenzi, L., Storti, F., Bistacchi, A., Toro, G., 2016. Structure of a normal seismogenic fault zone in carbonates: The Vado di Corno Fault, Campo Imperatore, Central Apennines (Italy). Journal of Structural Geology 90, 185–206.

Destro, N., 1995. Release fault: A variety of cross fault in linked extensional fault systems, in the Sergipe-Alagoas Basin, NE Brazil. Journal of Structural Geology 17, 615–629.

Devoti, R., Pietrantonio, G., Pisani, A., Riguzzi, F., Serpelloni, E., 2010. Present day kinematics of Italy. 36.

Di Domenica, A., Petricca, P., Trippetta, F., Carminati, E., Calamita, F., 2014. Investigating fault reactivation during multiple tectonic inversions through mechanical and numerical modeling: An application to the Central-Northern Apennines of Italy. Journal of Structural Geology 67, 167–185.

Dockrill, B., Shipton, Z.K., 2010. Structural controls on leakage from a natural CO2 geologic storage site: Central Utah, U.S.A. J. Struct. Geol. 32.

Doglioni, C., 1991. A proposal for the kinematic modelling of W dipping subductions possible applications to the Tyrrhenian Apennines system. Terra Nova 3, 423–434.

Ferrarini, F., Lavecchia, G., de Nardis, R., Brozzetti, F., 2015. Fault Geometry and Active Stress from Earthquakes and Field Geology Data Analysis: The Colfiorito 1997 and L’Aquila 2009 Cases (Central Italy). Pure and Applied Geophysics 172, 1079–1103.

Fossen, H., Johansen, T.E.S., Hesthammer, J., Rotevatn, A., 2005. Fault interaction in porous sandstone and implications for reservoir management; examples from Southern Utah. AAPG Bull. 89, 1593–1606.

Fossen, H., & Rotevatn, A. (2016). Fault linkage and relay structures in extensional settings—A review. Earth-Science Reviews, 154, 14-28.

Galadini, F., & Messina, P. (1994). Plio-Quaternary tectonics of the Fucino basin and surrounding areas (central Italy). Giornale di Geologia, 56(2), 73-99.

Galadini, F., Messina, P., 2001. Plio-Quaternary changes of the normal fault architecture in the Central Apennines (Italy). Geodinamica Acta 14, 321–344.

Gori, S., Falcucci, E., Ladina, C., Marzorati, S., Galadini, F., 2017. Active faulting, 3-D geological architecture and Plio-Quaternary structural evolution of extensional basins in the central Apennine chain, Italy. Solid Earth 8, 319–337.

Heidbach, O., Rajabi, M., Reiter, K., Moritz, WSM Team, 2016. World Stress Map Database Release 2016. GFZ Data Services.

Hodgetts, D., 2013. Laser scanning and digital outcrop geology in the petroleum industry: A review. Marine and Petroleum Geology 46, 335–354.

Hus, R., De Batist, M., Klerkx, J., & Matton, C. (2006). Fault linkage in continental rifts: structure and evolution of a large relay ramp in Zavarotny; Lake Baikal (Russia). Journal of structural geology, 28(7), 1338-1351.

Kattenhorn, S.A., Aydin, A., Pollard, D.D., 2000. Joints at high angles to normal fault strike: an explanation using 3-D numerical models of fault-perturbed stress fields. J. Struct. Geol. 22, 1–23.

Larsen, P. H. (1988). Relay structures in a Lower Permian basement-involved extension system, East Greenland. Journal of Structural Geology, 10(1), 3-8.

Lisle, R.J., Srivastava, D.C., 2004. Test of the frictional reactivation theory for faults and validity of fault-slip analysis. Geology 32, 569.

Long, J.J., Imber, J., 2012. Strain compatibility and fault linkage in relay zones on normal faults. Journal of Structural Geology 36, 16–26.

Marrett, R., Allmendinger, R.W., 1990. Kinematic analysis of fault-slip data. Journal of Structural Geology 973–986.

McCaffrey, K., Holdsworth, R., Imber, J., Clegg, P., De Paola, N., Jones, R., Hobbs, R., Holliman, N., Trinks, I., 2005a. Putting the geology back into Earth models. Eos, Transactions American Geophysical Union 86, 461–466.

McCaffrey, K.J.W., Jones, R.R., Holdsworth, R.E., Wilson, R.W., Clegg, P., Imber, J., Holliman, N., Trinks, I., 2005b. Unlocking the spatial dimension: digital technologies and the future of geoscience fieldwork. Journal of the Geological Society 162, 927–938.

Montone, P., Mariucci, T.M., Pondrelli, S., Amato, A., 2004. An improved stress map for Italy and surrounding regions (central Mediterranean). Journal of Geophysical Research: Solid Earth 109.

Morewood, N.C., Roberts, G.P., 2000. The geometry, kinematics and rates of deformation within an en échelon normal fault segment boundary, central Italy. Journal of Structural Geology 22, 1027–

1047.

Morris, A., Ferrill, D.A., Henderson, D.B., 1996. Slip-tendency analysis and fault reactivation. Geology 24, 275–278.

Patacca, E., Scandone, P., Di Luzio, E., Cavinato, G. P., & Parotto, M. (2008). Structural architecture of the central Apennines: Interpretation of the CROP 11 seismic profile from the Adriatic coast to the orographic divide. Tectonics, 27(3).

Peacock, D.C.P., Parfitt, E.A., 2002. Active relay ramps and normal fault propagation on Kilauea Volcano, Hawaii. J. Struct. Geol. 24, 729–742.

Peacock, D.C.P., Price, S.P., Pickles, C.S., 2000. The world's biggest relay ramp: hold with hope, NE Greenland. J. Struct. Geol. 22, 843–850.

Peacock, D. C. P., & Sanderson, D. J. (1991). Displacements, segment linkage and relay ramps in normal fault zones. Journal of Structural Geology, 13(6), 721-733.

Peacock, D. C. P., & Sanderson, D. J. (1994). Geometry and development of relay ramps in normal fault systems. AAPG bulletin, 78(2), 147-165.

Peacock, D.C.P., Dimmen, V., Rotevatn, A., Sanderson, D.J., 2017. A broader classification of damage zones. Journal of Structural Geology 102, 179–192.

Pless, J., McCaffrey, K., Jones, R., Holdsworth, R., Conway, A., Krabbendam, M., 2015. 3D characterization of fracture systems using Terrestrial Laser Scanning: an example from the

Lewisian basement of NW Scotland. Geological Society, London, Special Publications 421, 125–141.

Rotevatn, A., Buckley, S., Howell, J., Fossen, H., 2009. Overlapping faults and their effect on fluid flow in different reservoir types: A LIDAR-based outcrop modeling and flow simulation study. AAPG Bulletin 93, 407–427.

Rowland, J.V., Sibson, R.H., 2004. Structural controls on hydrothermal flow in a segmented rift system, Taupo Volcanic Zone, New Zealand. Geofluids 4, 259–283.

Scognamiglio, L., Tinti, E., Michelini, A., Dreger, D., Cirella, A., Cocco, M., Mazza, S., Piatanesi, A., 2010. Fast Determination of Moment Tensors and Rupture History: What Has Been Learned from the 6 April 2009 L'Aquila Earthquake Sequence. Seismological Research Letters 81, 892–906.

Seers, T., Hodgetts, D., 2016. Extraction of three-dimensional fracture trace maps from calibrated image sequences. Geosphere 12, 1323–1340.

Sibson, R.H., 1996. Structural permeability of fluid-driven fault-fracture meshes. J. Struct. Geol. 18, 1031–1042.

Smeraglia, L., Berra, F., Billi, A., Boschi, C., Carminati, E., Doglioni, C., 2016. Origin and role of fluids involved in the seismic cycle of extensional faults in carbonate rocks. Earth and Planetary Science Letters 450, 292–305.

Smeraglia, L., Bettucci, A., Billi, A., Carminati, E., Cavallo, A., Di Toro, G., Natali, M., Passeri, D., Rossi, M., Spagnuolo, E., 2017. Microstructural evidence for seismic and aseismic slips along clay-bearing, carbonate faults. Journal of Geophysical Research: Solid Earth, 122(5), 3895-3915.

Smith, S.A., Billi, A., Toro, G., Spiess, R., 2011. Principal Slip Zones in Limestone: Microstructural Characterization and Implications for the Seismic Cycle (Tre Monti Fault, Central Apennines, Italy). Pure and Applied Geophysics 168, 2365–2393.

Tavani, S., Granado, P., Corradetti, A., Girundo, M., Iannace, A., Arbués, P., ... & Mazzoli, S. (2014). Building a virtual outcrop, extracting geological information from it, and sharing the results in Google Earth via OpenPlot and Photoscan: An example from the Khaviz Anticline (Iran). Computers & Geosciences, 63, 44-53.

Telling, J, Lyda, A, Hartzell, P, Reviews, G.-C., 2017. Review of earth science research using terrestrial laser scanning. Earth-Science Reviews.

Tesei, T., Collettini, C., Barchi, M.R., Carpenter, B.M., Stefano, G., 2014. Heterogeneous strength and fault zone complexity of carbonate-bearing thrusts with possible implications for seismicity. 408, 307–318.

Thiele, S.T., Lachlan, Samsu, A., Micklethwaite, S., Voggler, S.A., Cruden, A.R., 2017. Rapid, semi-automatic fracture and contact mapping for point clouds, images and geophysical data. Solid Earth 8, 1241–1253.

Valoroso, L., Chiaraluce, L., Collettini, C., 2014. Earthquakes and fault zone structure. Geology 42, 343–346.

Wallace, R.E., 1951. Geometry of Shearing Stress and Relation to Faulting. The Journal of Geology 59, 118–130.

White, P.D., Jones, R.R., 2008. A cost-efficient solution to true color terrestrial laser scanning. Geosphere 4, 564.

Figure captions

Figure 1 – Structural setting of the Central Apennnines (A) and Plio-Quaternary tectonic evolution of the Fucino basin (B, C). The intermontane basins in the Central Apennines are commonly bordered by NW-SE and rarer WSW-ENE striking normal faults (red). Slip on normal faults accommodates a NE-SW oriented regional extension which started during late Miocene/early Pliocene and it is still ongoing, as testified by the stress field retrieved from recent seismic sequences (e.g., L'Aquila 2009; Scognamiglio et al., 2010; Ferrarini et al., 2015). The normal faults dismember a late Triassic to Miocene shallow-water to pelagic- carbonate succession shortened within the Apennines fold and thrusts belt. The Fucino Plain is an intermontane basin bordered by the Tre Monti fault (TMF) to NW and by the San Potito-Serrone fault system (SPSFS) to the NE. The San Potito – Serrone fault system comprises the San Potito-Celano (SPCF), Celano-Pescina (CPF), and Serrone (SF) faults. The tectonic evolution of the Fucino plain during early Pliocene time was controlled by dip-slip movements on the Tre Monti fault, which was longer at the time (B). Since Late Pliocene, the Fucino plain tectonics was controlled by NW-SE striking San Potito-Serrone fault system cutting the Tre Monti fault near the Celano village (C). Modified from Galadini and Messina, 1994.

Figure 2 – The Tre Monti fault. (A) Geological map of the Tre Monti area (modified from Smeraglia et al., 2016). The Tre Monti fault is ~7 km long and crops out in a series of SE-dipping

and right-stepping fault scarps. Mainly dip-slip kinematic indicators were observed on the main fault scarps, suggesting NW-SE oriented extensional stress field (stereoplot in Figure 2a). Blue and red dots in the stereoplot represent respectively the orientation of $\square_1$ and $\square_3$ inferred from the inversion of each slickenline. (B) Geological cross-section (section trace indicated in Figure 2a) showing that the Tre Monti fault is composed of a series of sub-parallel fault strands. The principal fault strand represents the tectonic contact between early Cretaceous to Miocene carbonates (footwall) and Pliocene to Quaternary deposits (hangingwall). (C) Zoom of the study-area marked with a black square in Figure 2a. The abandoned quarry is located at the footwall of the front segment in a relay ramp environment defined by two main right-stepping fault strands and exposes the damage zone within Early Cretaceous shallow-water limestones. The small black circle in Figure 2c represents the view point for Figure 4.

Figure 3 – Summary of the adopted methodology to build a 3D model representing the minor fault distribution in the abandoned quarry. A laser-scanner survey has been performed to produce a true-color point cloud. Using the CloudCompare software (www.cloudcompare.org), the minor faults were identified in the point cloud and manually picked to obtain a structural interpretation. Finally, we built a 3D model using the Move software.

Figure 4 – View of the abandoned quarry from the point indicated in Figure 2c. The main fault (front segment of the relay ramp) crops out in the western portion of the quarry where it puts in contact the Early Cretaceous shallow-water limestones in the footwall, with Pleistocene continental breccias (“Brecce Rosate” Unit; Cavinato et al., 2002) in the hangingwall. The damage zone is located in Early Cretaceous shallow-water limestones and characterized by pervasive fracturing and the presence of minor faults. The fault is characterized by right-lateral kinematic indicators providing the stress field reported in the stereoplot (Schmidt net lower hemisphere). Blue and red

dots in the stereoplot represent respectively the calculated σ_1 and σ_3 orientation for each slickenline.

Figure 5 – Minor faults map obtained from the manual interpretation of the virtual outcrop. Minor faults are heterogeneously distributed within the damage zone, with the highest concentration in the northern sector of the quarry. The minor faults attitudes obtained from both the real and the virtual outcrop are represented as poles in the two stereoplot (Schmidt net lower hemisphere). The black line (AB) represent the trace of the cross-section reported in Figure 6. The black dots with yellow triangles indicate view points for Figure 6a and 6b.

Figure 6 – Minor faults in the abandoned quarry. A) Faults striking subparallel to the main fault are the most abundant and are often characterized by two slickenlines sets (inset). This set is accompanied by smaller faults striking orthogonal to the main fault (B). C) Vertical cross-section parallel to the main fault dip. The outcrop-scale internal structure for the Tre Monti fault is depicted by the minor fault distribution, characterized by major fault strands sub-parallel to the main fault with smaller faults with different orientation.

Figure 7 – Minor faults kinematics. (A) Density contour plot of slickenlines (Schmidt net, lower emisphere). The slickenlines point toward all directions, with maximum densities toward WSW, W, and NW. (B) Bar charts showing the distribution of fault orientation and kinematics. The faults exhibit various kinematics for each fixed orientation. (C) Stereoplot (Schmidt net, lower emisphere) of minor faults for left (red), normal (orange), and right main slip component.

Figure 8 – Normalised slip tendency and slickenlines compatibility analysis for three hypothesized stress fields: active regional NE-SW orientated extension (regional stress field; A), NW-SE oriented

extension (fault stress field; B) compatible with the mainly dip-slip slickenlines observed for the whole Tre Monti fault, and a quarry stress field (C) calculated from the inversion of the right-lateral slickenlines observed on the front segment of the relay ramp. Black dots in the slip tendency stereoplots represent the poles to the minor faults. The slip tendency stereoplots have been produced using a MATLAB tool for slip tendency (Bistacchi et al., 2012). Green and Red colours in the slickenlines compatibility stereoplots represent respectively compatible and non-compatible slickenlines with respect to the predicted slickenlines orientation in a given stress field.

Figure 9 – Interpretation of the complex kinematics of minor faults. Minor faults geometry and kinematics reflect the local-scale temporal interaction between various stress fields. (A) a NE-SW oriented extension acting at regional scale (i.e., regional stress field), and (B) a NW-SE oriented extension (fault stress field) at sub-regional scale (10 km scale), due to the release fault geometry of the Tre Monti fault add further geometrical and kinematic complexity to (C) a quarry stress field due to the interaction of two main fault strands that borders the quarry.

Table 1 – Parameters defining the stress fields assumed for the kinematic analysis of minor fault slickenlines.

Table 2 – Results for the slip tendency and slickenline compatibility analysis for different fault orientations.

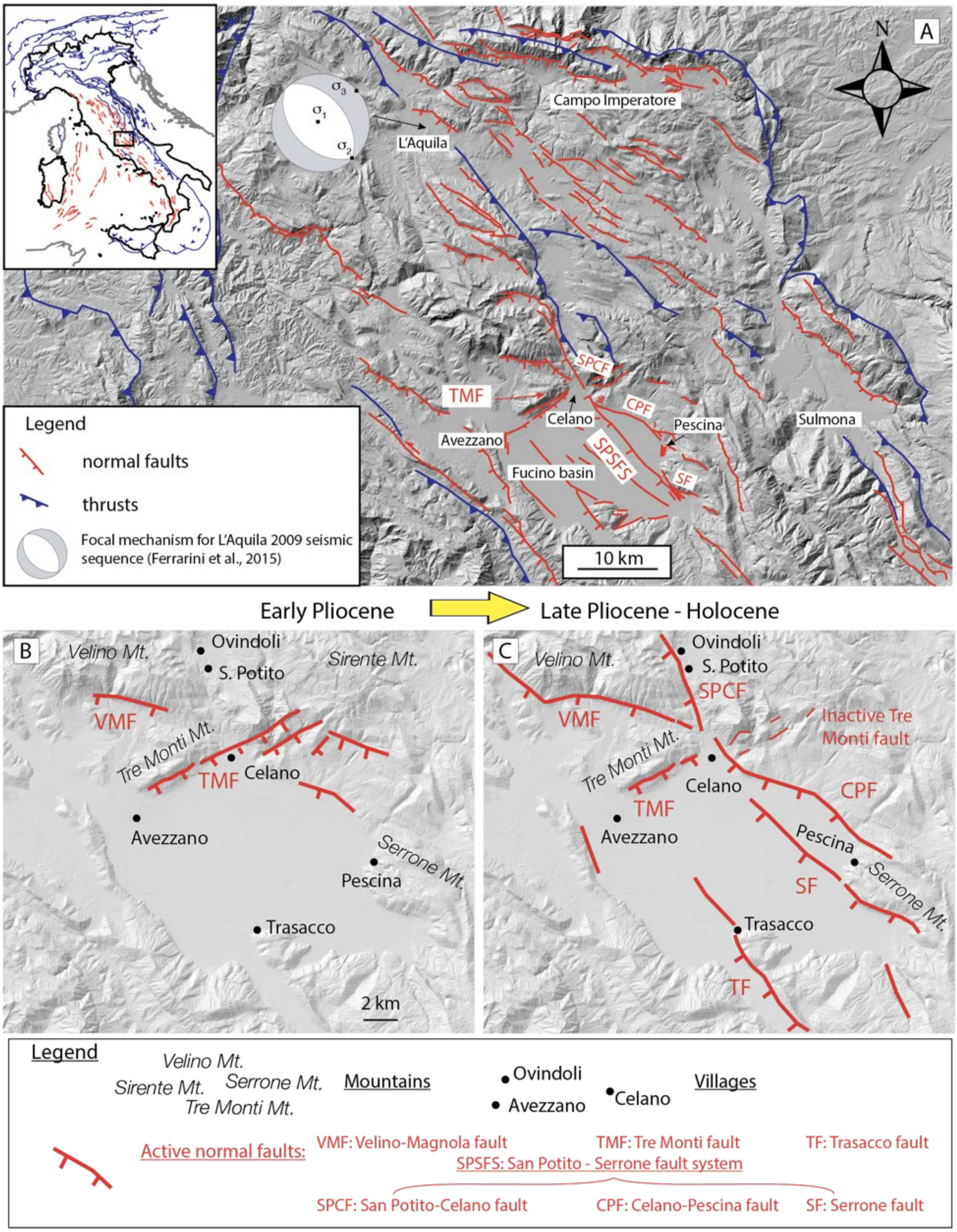

Figure 1 – Structural setting of the Central Apennnines (A) and Plio-Quaternary tectonic evolution of the Fucino basin (B, C). The intermontane basins in the Central Apennines are commonly bordered by NW-SE and rarer WSW-ENE striking normal faults. Slip on normal faults accommodates a NE-SW oriented regional extension which started during late Miocene/early Pliocene and it is still ongoing, as testified by the stress field retrieved from recent seismic sequences (e.g., L'Aquila 2009; Scognamiglio et al., 2010; Ferrarini et al., 2015). The normal faults dismember a late Triassic to Miocene shallow-water to pelagic- carbonate succession shortened

within the Apennines fold and thrusts belt. The Fucino Plain is an intermontane basin bordered by the Tre Monti fault (TMF) to NW and by the San Potito-Serrone fault system (SPSFS) to the NE. The San Potito-Serrone fault system comprises the San Potito–Celano (SPCF), Celano-Pescina (CPF), and Serrone (SF) faults. The tectonic evolution of the Fucino plain during early Pliocene time was controlled by dip-slip movements on the Tre Monti fault, which was longer at the time (B). Since Late Pliocene, the Fucino plain tectonics was controlled by NW-SE striking San Potito – Serrone fault system cutting the Tre Monti fault near the Celano village (C). Modified from Galadini and Messina, 1994.

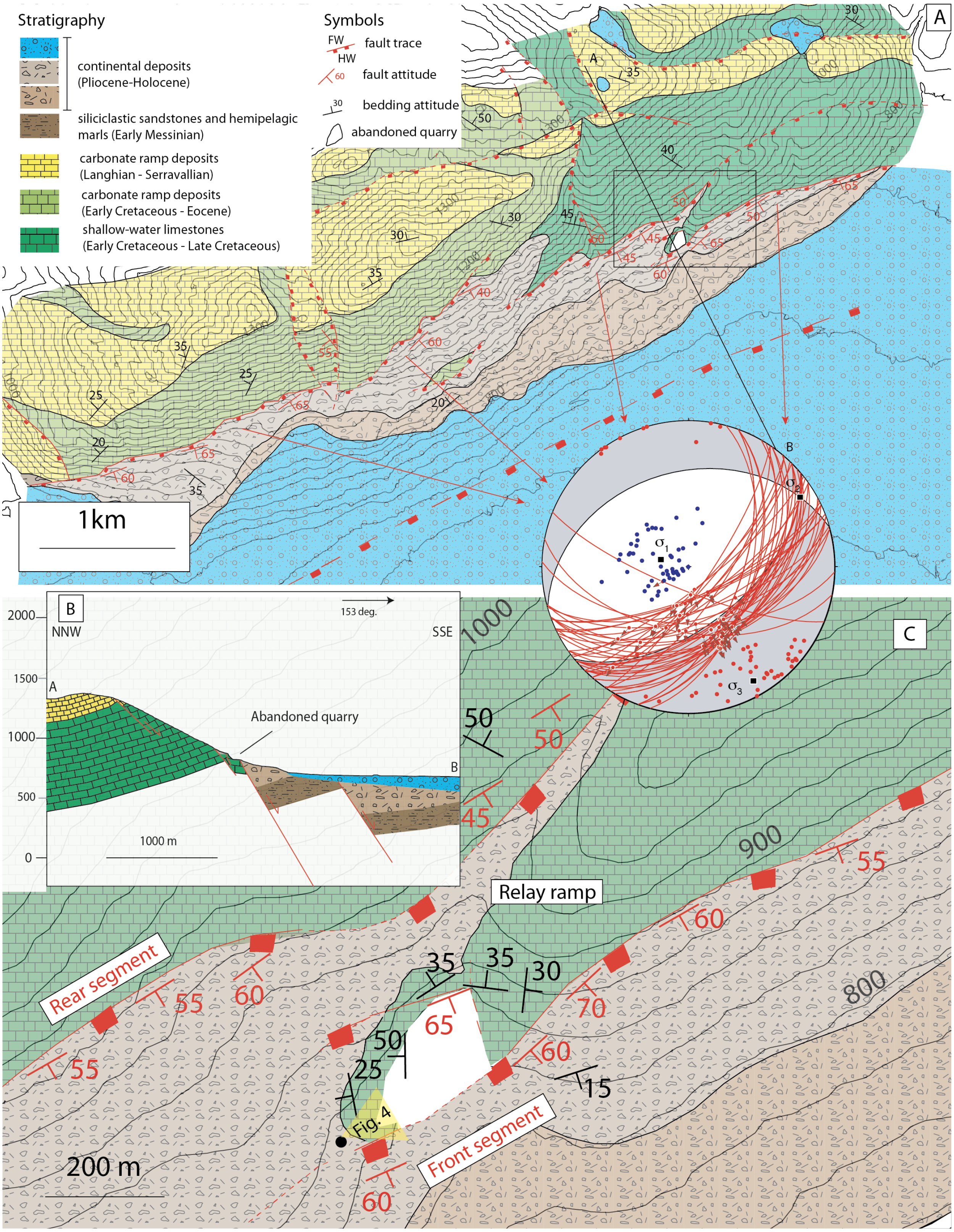

Figure 2 – The Tre Monti fault. (A) Geological map of the Tre Monti area (modified from Smeraglia et al., 2016). The Tre Monti fault is ~7 km long and crops out in a series of SE-dipping and right-stepping fault scarps. Mainly dip-slip kinematic indicators were observed on the main fault scarps, suggesting NW-SE oriented extensional stress field (stereoplot in Figure 2a). Blue and red dots in the stereoplot represent respectively the orientation of σ_1 and σ_3 inferred from the inversion of each slickenline. (B) Geological cross-section (section trace indicated in Figure 2a) showing that the Tre Monti fault is composed of a series of sub-parallel fault strands. The principal

fault strand represents the tectonic contact between early Cretaceous to Miocene carbonates (footwall) and Pliocene to Quaternary deposits (hangingwall). (C) Zoom of the study-area marked with a black square in Figure 2a. The abandoned quarry is located at the footwall of the front segment in a relay ramp environment defined by two main right-stepping fault strands and exposes the damage zone within Early Cretaceous shallow-water limestones. The small black circle in Figure 2c represents the view point for Figure 4.

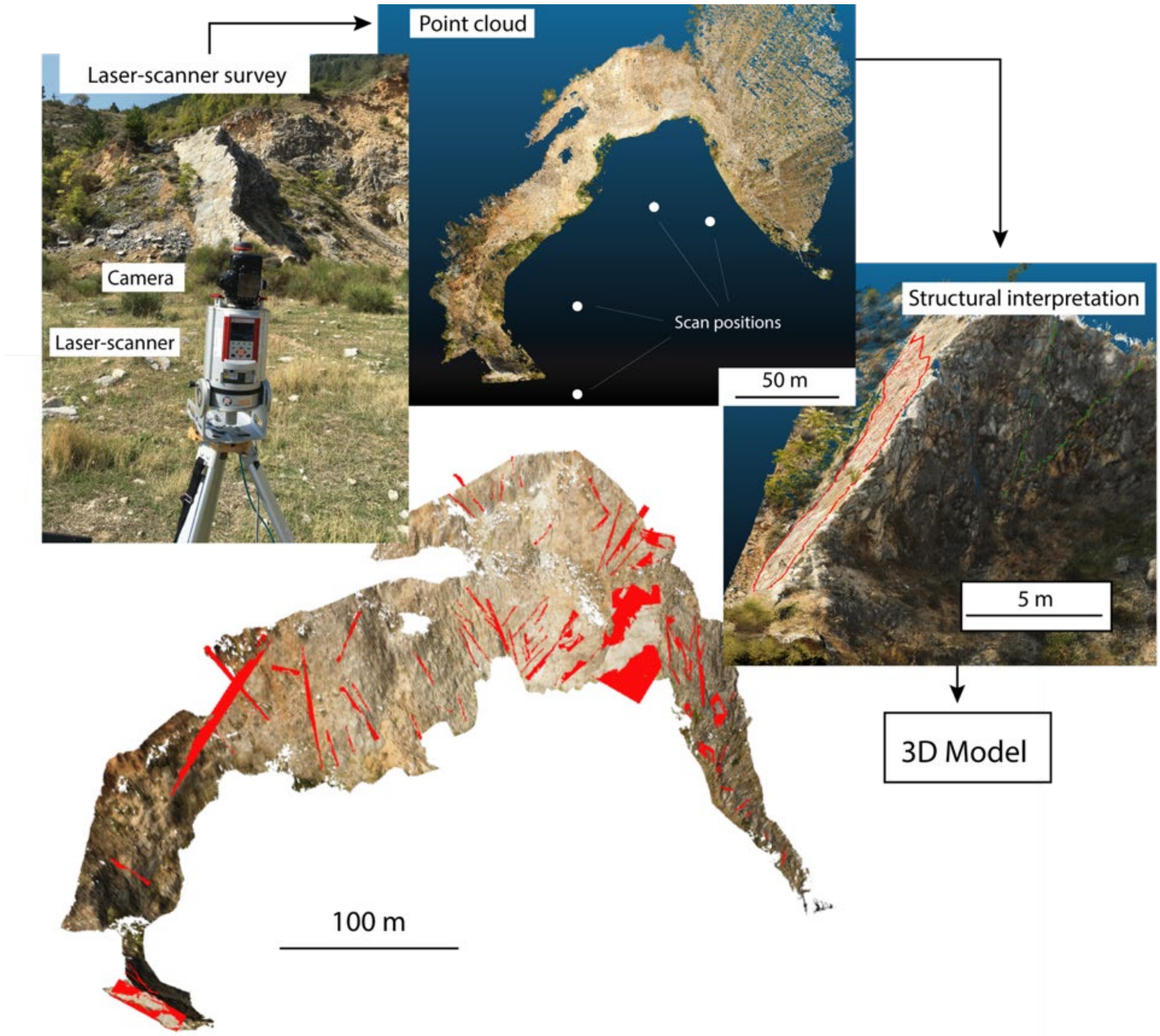

Figure 3– Summary of the adopted methodology to build a 3D model representing the minor fault distribution in the abandoned quarry. A laser-scanner survey has been performed to produce a true-color point cloud. Using the CloudCompare software (www.cloudcompare.org), the minor faults were identified in the point cloud and manually picked to obtain a structural interpretation. Finally, we built a 3D model using the Move software.

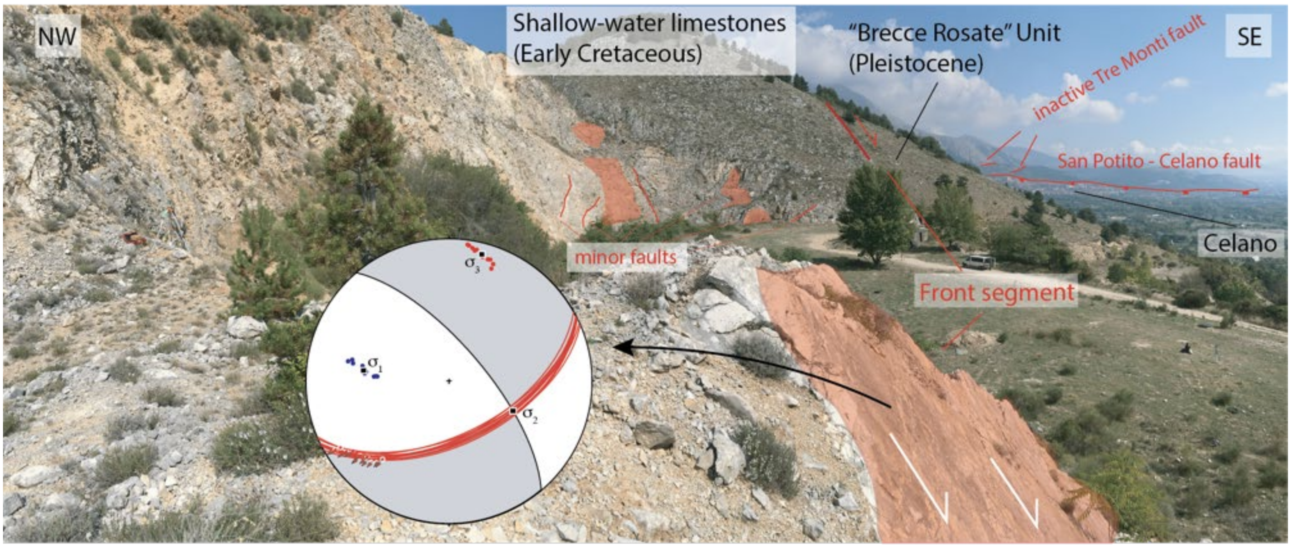

Figure 4 – View of the abandoned quarry from the point indicated in Figure 2c. The main fault (front segment of the relay ramp) crops out in the western portion of the quarry where it puts in contact the Early Cretaceous shallow-water limestones in the footwall, with Pleistocene continental breccias ("Brecce Rosate" Unit; Cavinato et al., 2002) in the hangingwall. The damage zone is located in Early Cretaceous shallow-water limestones and characterized by pervasive fracturing and the presence of minor faults. The fault is characterized by right-lateral kinematic indicators providing the stress field reported in the stereoplot (Schmidt net lower hemisphere). Blue and red dots in the stereoplot represent respectively the calculated σ_1 and σ_3 orientation for each slickenline.

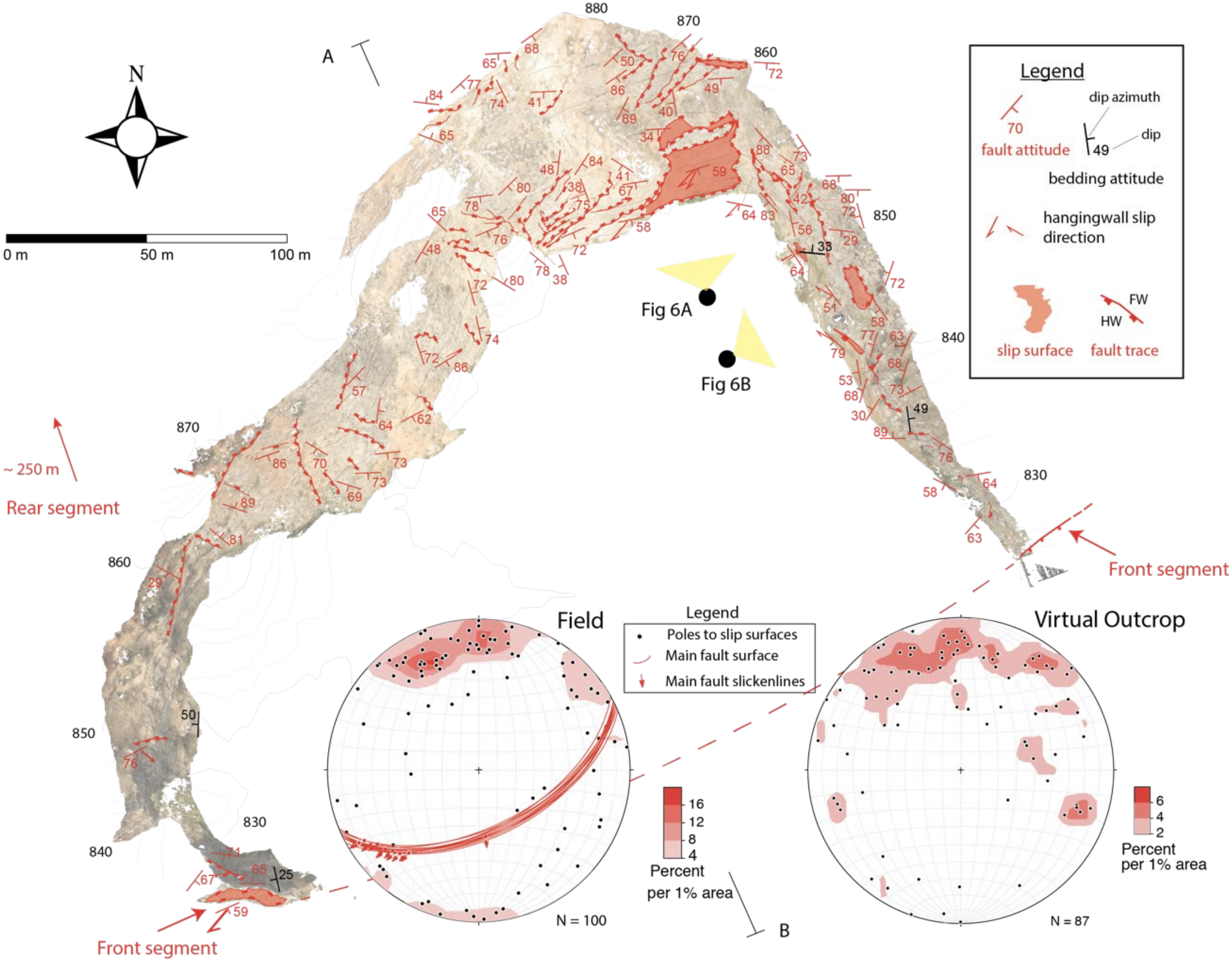
A
B
N
0 m
50 m
100 m
Legend
70
fault attitude
dip azimuth
dip
49
bedding attitude
hangingwall slip direction
FW
HW
slip surface
fault trace
Fig 6A
Fig 6B
~ 250 m
Rear segment
Front segment
Front segment
Field
Virtual Outcrop
Legend
Poles to slip surfaces
Main fault surface
Main fault slickenlines
16
12
8
4
Percent per 1% area
6
4
2
Percent per 1% area
N = 100
N = 87

Figure 5 – Minor faults map obtained from the manual interpretation of the Virtual Outcrop. Minor faults are heterogeneously distributed within the damage zone, with the highest concentration in the northern sector of the quarry. The minor faults attitudes obtained from both the real and the virtual outcrop are represented as poles in the two stereoplot (Schmidt net lower hemisphere). The black line (AB) represent the trace of the cross-section reported in Figure 6. The black dots with yellow triangles indicate view points for Figure 6a and 6b.

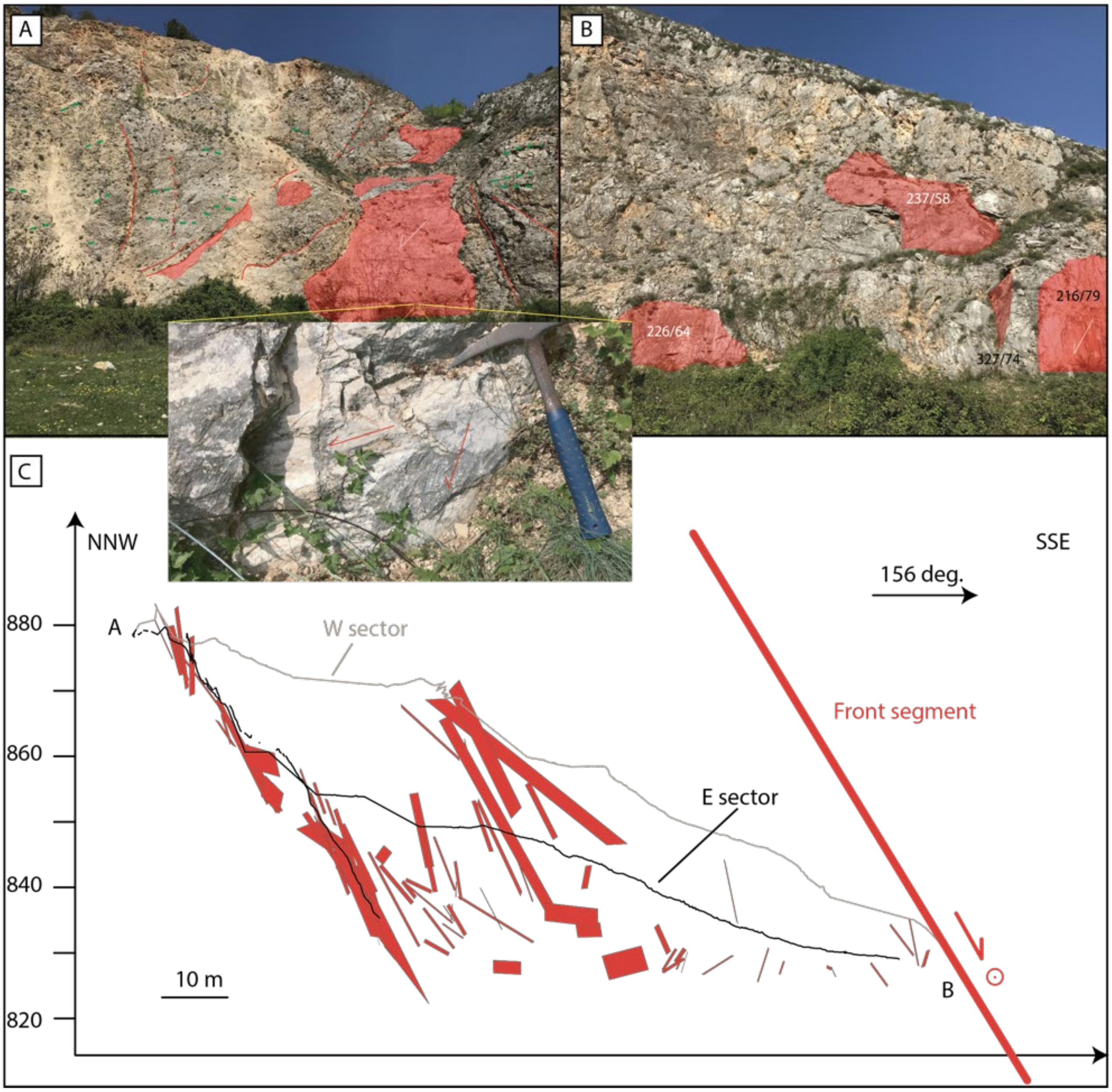

Figure 6 – Minor faults in the abandoned quarry. A) Faults striking subparallel to the main fault are the most abundant and are often characterized by two slickenlines sets (inset). This set is accompanied by smaller faults striking orthogonal to the main fault (B). C) Vertical cross-section parallel to the main fault dip. The outcrop-scale internal structure for the Tre Monti fault is depicted by the minor fault distribution, characterized by major fault strands sub-parallel to the main fault with smaller faults with different orientation.

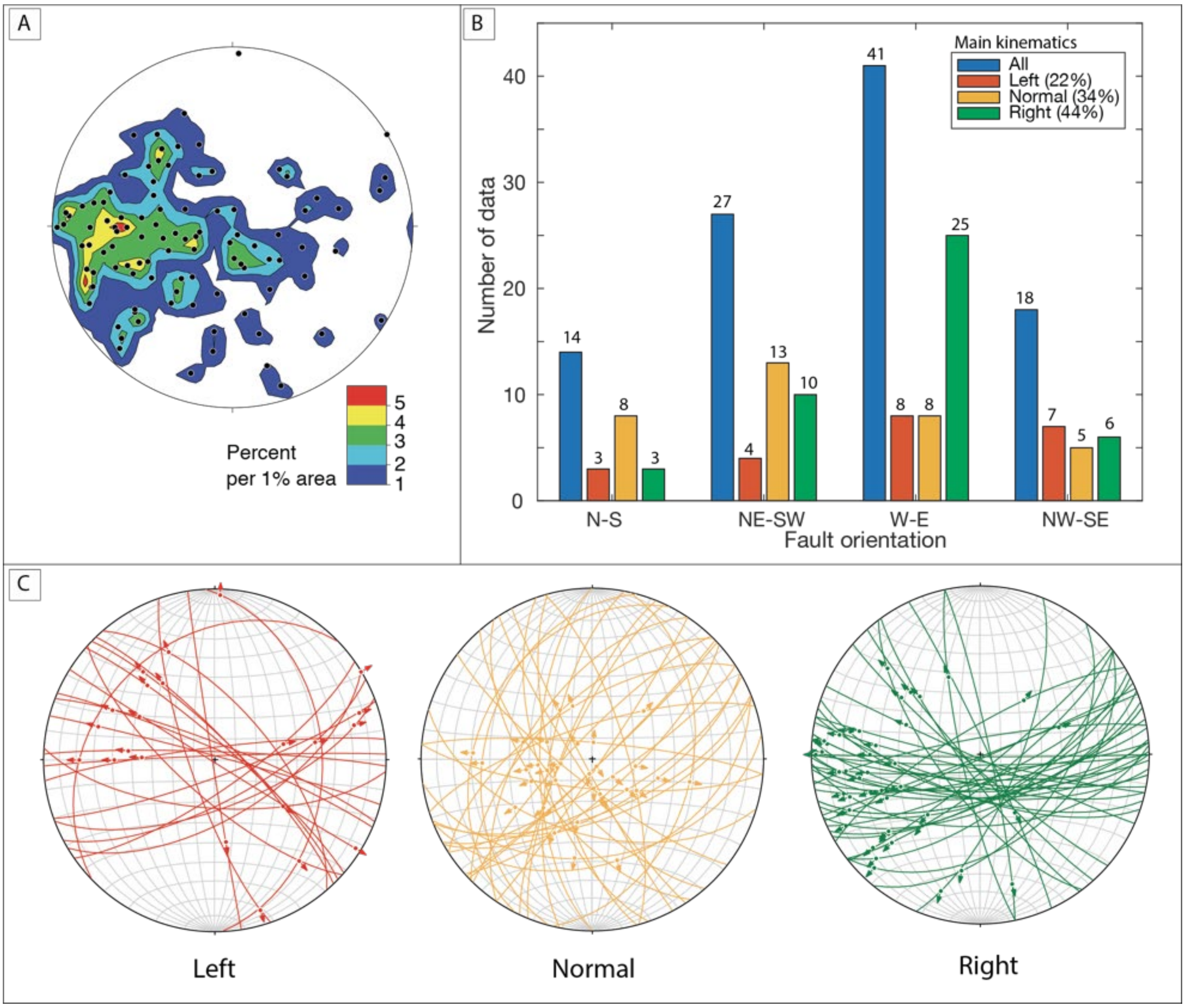

Figure 7 – Minor faults kinematics. (A) Density contour plot of slickenlines (Schmidt net, lower emisphere). The slickenlines point toward all directions, with maximum densities toward WSW, W, and NW. (B) Bar charts showing the distribution of fault orientation and kinematics. The faults exhibit various kinematics for each fixed orientation. (C) Stereoplot (Schmidt net, lower emisphere) of minor faults for left (red), normal (orange), and right main slip component.

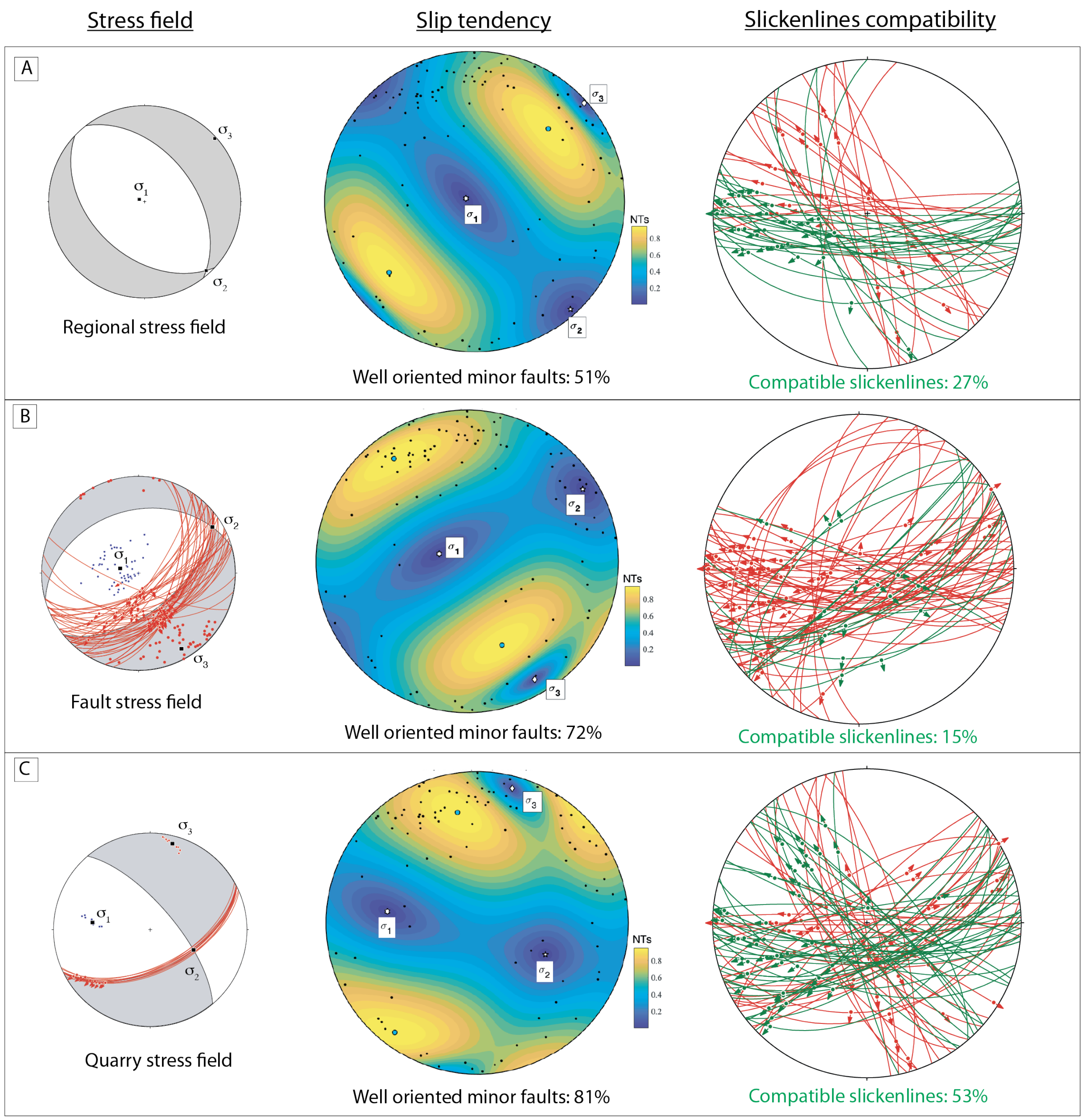

Figure 8 – Normalised slip tendency and slickenlines compatibility analysis for three hypothesized stress fields: active regional NE-SW orientated extension (regional stress field; A), NW-SE oriented extension (fault stress field; B) compatible with the mainly dip-slip slickenlines observed for the whole Tre Monti fault, and a quarry stress field (C) calculated from the inversion of the right-lateral slickenlines observed on the front segment of the relay ramp. Black dots in the slip tendency stereoplots represent the poles to the minor faults. The slip tendency stereoplots have been produced using a MATLAB tool for slip tendency (Bistacchi et al., 2012). Green and Red colours in the slickenlines compatibility stereoplots represent respectively compatible and non-compatible slickenlines with respect to the predicted slickenlines orientation in a given stress field.

Stress field name	$\boldsymbol{\sigma_1}$ **(trend/plunge)**	$\boldsymbol{\sigma_3}$ **(trend/plunge)**	**Stress shape ratio ($\boldsymbol{\phi}$)**	**Friction coefficient**
Regional stress field	292/85	048/02	0.56 (Ferrarini et al., 2015)	0.6
Fault stress field	285/74	150/11	0.56 (Ferrarini et al., 2015)	0.6
Quarry stress field	277/39	015/09	0.56 (Ferrarini et al., 2015)	0.6

Table 1 – Parameters defining the stress fields assumed for the kinematic analysis of minor fault slickenlines.

Strike	Abundance	Well-oriented			Slickenlines compatibility		
		Regional	Fault	Quarry	Regional	Fault	Quarry
E-W	41%	29%	41%	36%	22%	5%	23%
NE-SW	27%	0%	26%	20%	0%	9%	9%
NW-SE	18%	12%	2%	18%	2%	3%	10%
N-S	14%	10%	5%	7%	3%	0%	1%
all	100%	51%	72%	81%	27%	15%	53%

Table 2 – Results for the slip tendency and slickenline compatibility analysis for different fault orientation.

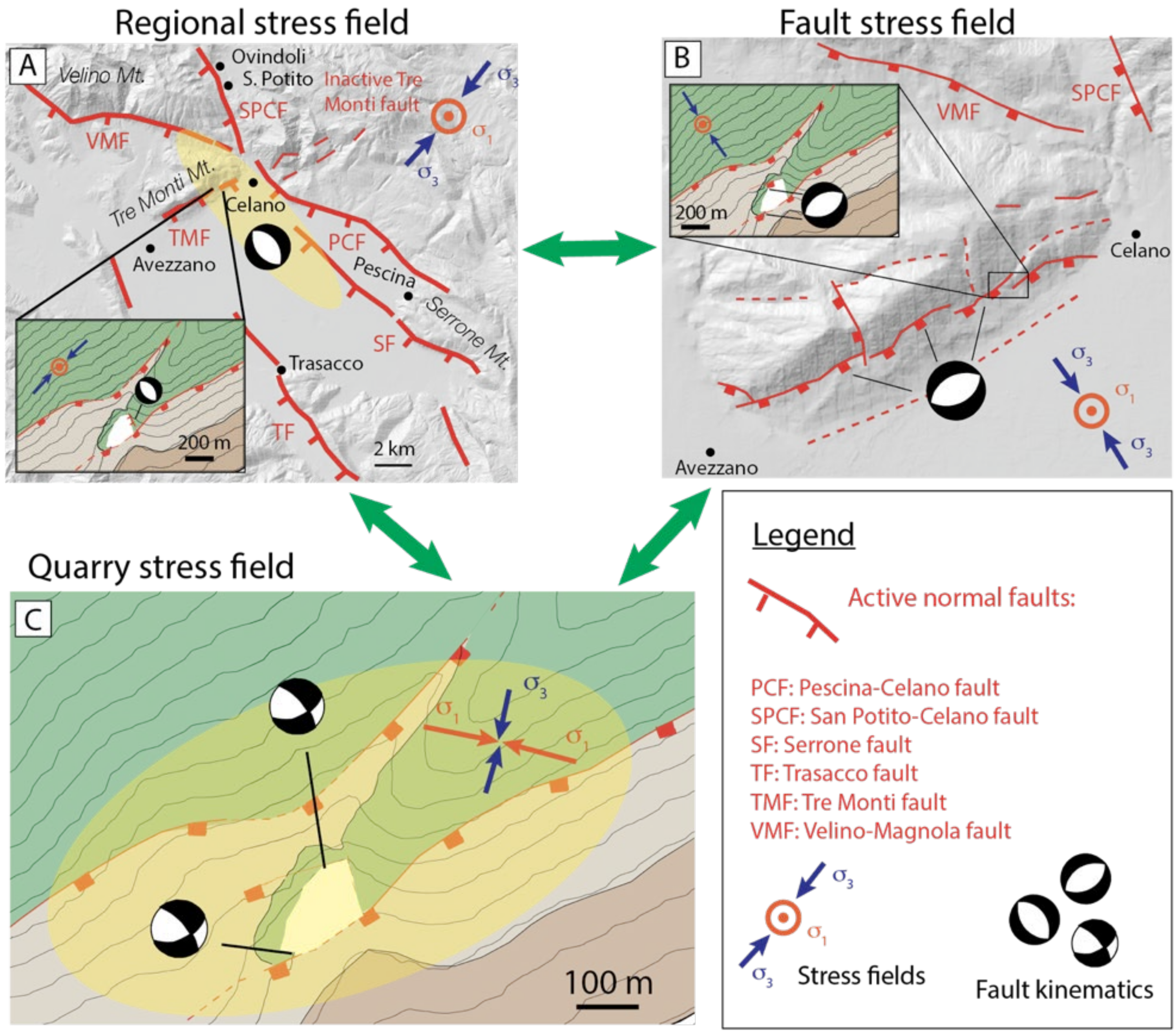

Figure 9 – Interpretation of the complex kinematics of minor faults. Minor faults geometry and kinematics reflect the local-scale temporal interaction between various stress fields. (A) a NE-SW orientated extension acting at regional scale (i.e., regional stress field), and (B) a NW-SE oriented extension (fault stress field) at sub-regional scale (10 km scale), due to the release fault geometry of the Tre Monti fault add further geometrical and kinematical complexity to (C) a quarry stress field due to the interaction of two main fault strands that borders the quarry.